

Ultrafine and Smooth Full Metal Nanostructures for Plasmonics

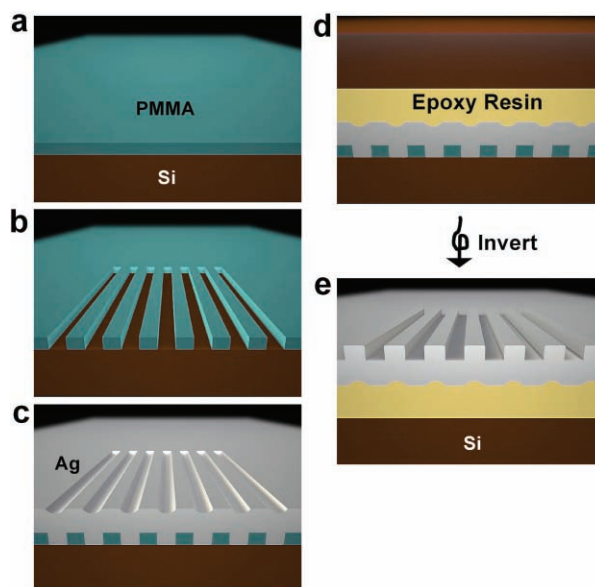
By Xinli Zhu, Yang Zhang, Jiasen Zhang,* Jun Xu, Yue Ma, Zhiyuan Li, and Dapeng Yu*

Surface plasmon polaritons (SPPs) are light waves coupled with free electron oscillations bound to a metal-dielectric interface.^[1] They have many fascinating features such as strong field confinement at the nanoscale, intensive local field enhancement, and interplay between strongly localized and propagating SPPs. For these reasons they promise great potentials in various optical applications.^[2–6] The SPPs can be excited, guided, focused, and confined by a textured metal surface.^[7,8] However, the involuntary surface roughness, which inevitably exists using traditional fabrication processes,^[9,10] increases the propagation loss. Therefore, the fabrication of sufficiently smooth metal surface with nanoscale feature size is crucial for SPPs to have practical applications. A broad spectrum of techniques, including focused ion beam (FIB) milling,^[11] electron beam lithography (EBL),^[8] nanoimprinting,^[12] and interference lithography,^[13] have been developed to ensure precise and easy fabrication. However, FIB is costly, time-consuming, impurity-implanted with unbearable rough surface, while lift-off or etching processes followed by metal depositions undermines the resolution of the nanostructures with rough surface and can generate contamination. Furthermore, these techniques can hardly produce a metal surface with desirable smoothness. Achieving full metal SPP nanostructures with exceptionally smooth surface and high aspect ratio remains a great challenge.

The template stripping (TS) method is a simple technique usually used to obtain ultra-flat surfaces,^[14,15] make patterns on mica,^[16] and create ultra-flat patterned metal surfaces.^[3,17] However, the patterned metal films with controllable shapes and sizes, in particularly at nanoscale, are required for plasmonic applications. In this communication, we combine TS method with EBL-patterned poly (methyl methacrylate) (PMMA) layer as a template to fabricate high quality metal nanostructures with ultrasmooth surface and high aspect ratio. The simple fabrication process was described as follows: PMMA with desired thickness was spun on silicon wafer (Scheme 1a) and then exposed and developed into designed nanostructures via EBL (Scheme 1b). A metal layer, which was thicker than the PMMA layer to ensure complete coverage, was then deposited on the negative

patterns by magnetron sputtering deposition (Scheme 1c). After being glued to another silicon substrate with an epoxy resin adhesive (Scheme 1d), the metal layer was easily stripped off the PMMA/silicon wafer due to the weak adhesion between the metal layer and the PMMA. After cleansing the residual PMMA with acetone, the resulting top metal layer inherited completely the morphology and the smoothness of the PMMA patterns (Scheme 1e). By using this method, the surface smoothness of silicon wafer and the PMMA was faithfully transferred to the metal film. The advantages of the PMMA-based TS method are summarized as follows: 1) The metal nanostructures fabricated precisely replicate the patterns designed on the PMMA layer. Therefore, EBL-defined PMMA patterns can be well reserved in the metal film. 2) The metal surface is ultra smooth because it inherits the surface smoothness of the silicon wafer or PMMA layer. 3) A precipitous top-to-bottom profile can be obtained with a very high aspect ratio. The desired height of the metal structures can be simply obtained by changing the thickness of PMMA layer. 4) The shape, size, and spacing of the metal patterns can be precisely controlled in three dimensions due to the flexibility of EBL.

The surface roughness of the metal structure fabricated via our technique was found to be at the angstrom level, which



Scheme 1. Schematic diagram of the fabrication process of metal patterns by means of PMMA-based TS method. (a) A silicon wafer is spin-coated by PMMA. (b) PMMA is patterned by standard EBL. (c) A metal layer is deposited on patterned PMMA. (d) The metal layer is glued to another substrate. (e) The sample is turned upside down after the first substrate is stripped off and residual PMMA is rinsed with acetone.

[*] X. L. Zhu, Y. Zhang, Prof. J. S. Zhang, J. Xu, Y. Ma, Prof. D. P. Yu
State Key Laboratory for Mesoscopic Physics
Department of Physics
Peking University
Beijing 100871 (P. R. China)
E-mail: jszhang@pku.edu.cn; yudp@pku.edu.cn

Prof. Z. Y. Li
Institute of Physics
Chinese Academy of Sciences
Beijing 100190 (P. R. China)

DOI: 10.1002/adma.201001313

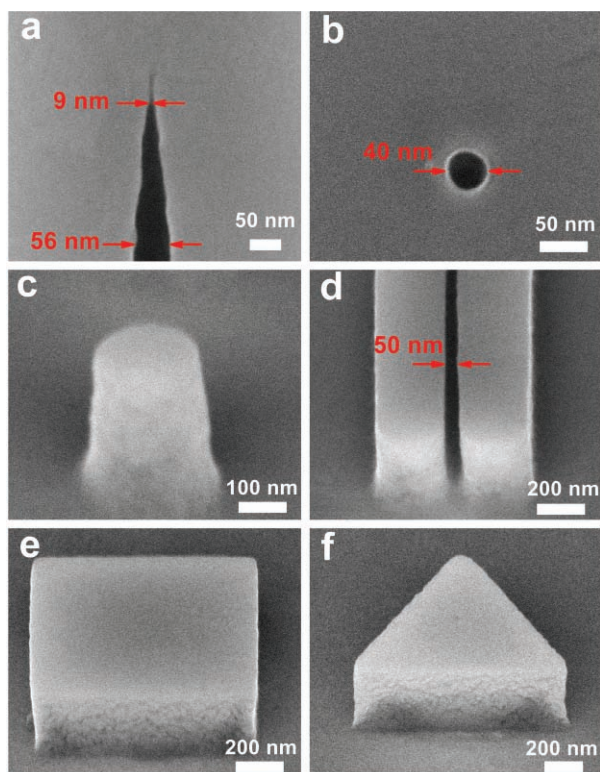


Figure 1. Typical SEM images of various single structural elements on silver film. The height of all the patterns is 300 nm. (a) A single hole in 40 nm diameter. (b) Tapered structure with a gap down to 9 nm. (c) A pillar in 220 nm diameter. (d) A 50-nm-wide groove. (e) A 960 nm side length square-shaped bump. (f) A 900-nm side length equilateral-triangle bump.

was confirmed by using an atomic force microscope. The root-mean-square (RMS) roughness of the PMMA layer and silicon wafer is 0.28 and 0.21 nm, respectively (Supporting Information, Figure S1a and b). The RMS roughness of the metal surface in the unexposed and exposed regions is 0.88 and 0.55 nm (Supporting Information, Figure S1c and d), which is close to that of the PMMA surface and the silicon wafer, respectively. In sharp contrast, the RMS roughness of the top surface of the metal film (1 μm thick) directly deposited on the silicon wafer and the PMMA film without using our transfer method is 5.2 and 3.7 nm, respectively (Supporting Information, Figure S1e and f). Therefore, it was very difficult to decrease the roughness to the level of the flat PMMA layer or the silicon wafer surface by direct metal deposition using other methods.

To demonstrate the great potential of our method, we have fabricated a variety of silver plasmonic nanostructures by means of the PMMA-based TS method. Their morphologies were examined by using scanning electron microscope (SEM), as are shown in **Figure 1**. The smallest gap has a size only ~ 9 nm (Figure 1a), which is down to the EBL resolution limit of our equipment. The aspect ratio is larger than 20 for the gap. Single well and pillar structures (Figure 1b and c) also have a good profile as well as a small feature size. The deep groove (Figure 1d) has a width as small as 50 nm, which can act as a nanosize plasmonic waveguide, and can confine the electromagnetic field intensively. In order to obtain a sharp angle, larger size structures

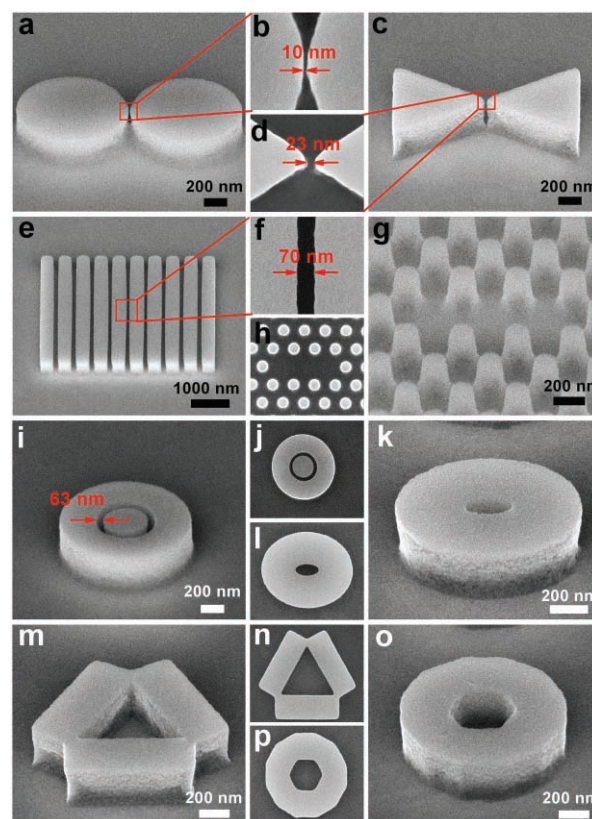


Figure 2. Typical SEM images of various silver nanostructures. The height of all the patterns is 300 nm. (a,b) A 975 nm-diameter cylinder pair with a 10 nm gap. (c,d) A 920 nm-side length equilateral-triangle bump pair with a 23 nm gap. (e,f) A grating with a 455 nm pitch and a 70-nm-wide groove. (g,h) A hexagonal array of 180 nm-diameter nano-pillars spaced by 375 nm (center to center). (i,j) Coaxial cylinders separated by a 63 nm annular-shaped groove. (k,l) An elliptical-shaped plasmonic cavity with a 125 nm short axis and a 245 nm long axis. (m,n) An equilateral-triangle plasmonic cavity with a 705 nm side length. (o,p) An equilateral-hexagonal plasmonic cavity with a 225 nm side length.

are needed (Figure 1e and f). It is clearly demonstrated that the nanoscale plasmonic structures fabricated by our technique can achieve very smooth and precipitous top-to-bottom profiles at nanoscale feature size. These characteristics are crucial to the propagation, confinement and actual applications of the SPPs.

Due to the flexibility of the present technique, more complicated structures can be fabricated with different shapes, sizes, and spacings. **Figure 2a–d** show the fabricated optical nanoantennas: a cylinder pair with 10 nm gap and a “bowtie” antenna with 23 nm gap. The small gap is very important for local field enhancement.^[18,19] The gap spacing can be precisely changed using our method in order to tune the properties of the antenna. One- and two-dimensional SPP photonic crystal structures are shown in Figure 2e–h.^[20,21] The high aspect ratio and ultra-smooth surface can help to create large band gaps and maintain low propagation loss. Another important application of our method is in the fabrication of plasmonic nanocavities with metal reflectors. The silver walls provide omnidirectional broadband reflectors with high reflectivity. We have made several kinds of the plasmonic cavities, including the whispering

gallery^[22] (Figure 2i and j), elliptical (Figure 2k and l), equilateral-triangle (Figure 2m and n), and hexagonal (Figure 2o and p) cavities. The ultrasmooth surface of the plasmonic cavities fabricated by our method guarantee very high reflectivity and low propagation loss, which result in a high quality factor (*Q*-factor) for confined plasmonic modes. The height of the metal structures is easy to change by varying the thickness of the PMMA layer. SPP nanostructures with different heights from 60 to 600 nm have also been fabricated (Supporting Information, Figure S2 and S3).

To manifest the advantages of our technique with exceptional SPP performance, we systematically investigated the plasmonic resonance modes confined in equilateral-triangle cavities with 300 nm high silver reflectors. The SPPs are directly excited by electron beam source. The emitted spectra and field intensity profile of the plasmonic modes in the cavity were measured and imaged by using a high spatial and spectral resolution cathodoluminescence (CL) spectroscopy.^[9,23] The panchromatic CL collecting mode can reveal the energy spectra at the excited location, while the monochromatic CL collecting mode can image the field intensity profile of the plasmonic modes within the whole cavity. The panchromatic CL spectrum measured in an equilateral-triangle cavity with side lengths $a = 935$ nm exhibits three distinct resonant peaks at 452, 580, and 818 nm (Figure 3a). As the side length decreases, the number of resonant peaks decreases, and only a single mode exists for the cavities with side length $a = 500$ and 430 nm (Supporting Information, Figure S4). Moreover, the spatially resolved CL mappings of the cavity imaged at each corresponding resonant wavelength were conducted and shown in Figure 3b–d. The brightness corresponds to the emitted photon intensity. In order to determine the origin of the observed SPP modes, the finite-difference time-domain (FDTD) technique is used to calculate the plasmonic modes in such a cavity. The mode intensity of the in-plane and out-of-plane electric field components of SPPs at a vacuum wavelength of 818 nm is shown in Figure S5a and b (Supporting Information), respectively. There is a good agreement between the calculation and the experimental data, which reveals that the modes directly observed in the CL mapping experiments correspond to the out-of-plane component of the plasmonic modes. It can be seen that the intensity of the mode in Figure 3b–d is ~ 0 at the boundary of the cavity, revealing that the phase shift $\Delta\phi$ upon reflection is $\sim \pi$. This is consistent with the FDTD simulation of the reflection phase shift of the out-of-plane component (Supporting Information, Figure S5c).

In order to determine the modes in Figure 3b–d, the field patterns of the modes (1, 3), (1, 5), (2, 4), (1, 7), and (3, 5) of an equilateral-triangle cavity with the boundary condition $E = 0$ are calculated and shown in Figure 3e–g, respectively.^[24] The three resonant wavelengths 818, 580, and 452 nm can be assigned well to the mode (1, 3), the degenerate modes (1, 5) and (2, 4), and the degenerate modes (1, 7) and (3, 5), respectively. The corresponding theoretical resonant wavelengths with a side length of 935 nm and the boundary condition $E = 0$ are 810, 530, and 389 nm, respectively, which are slightly different from the experimental SPP resonant wavelengths of 806, 560, and 419 nm. The *Q*-factor of the modes can be obtained from Figure 3a directly, and they are 12, 21, and 10 at 452, 580, and 818 nm, respectively. The clear mode patterns and the relatively high

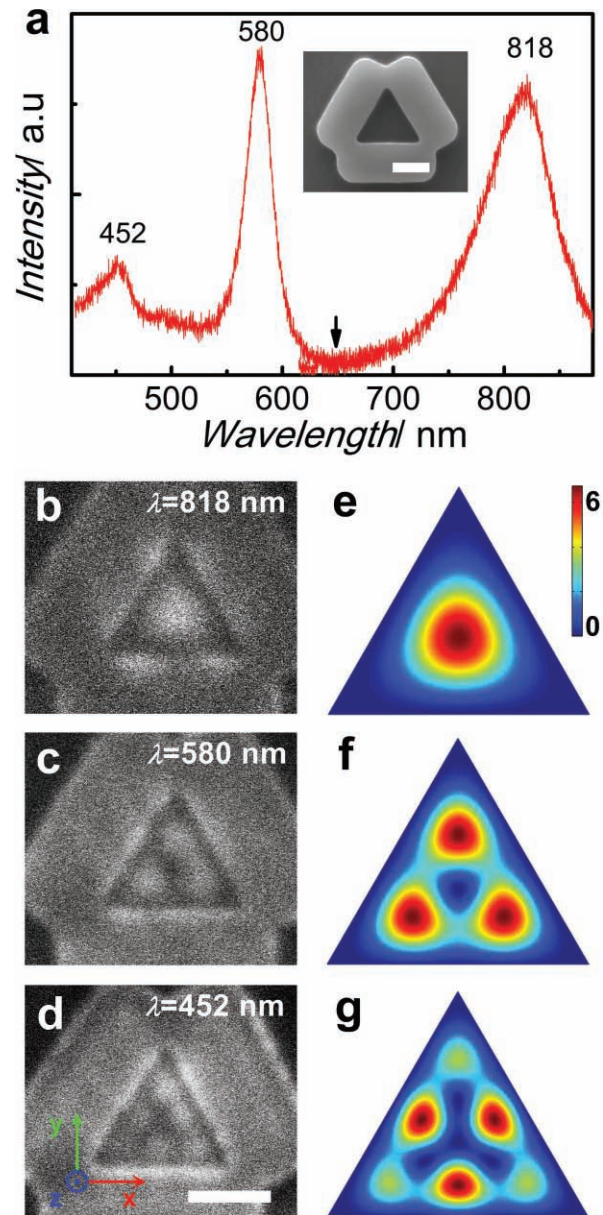


Figure 3. Panchromatic CL spectrum and mode patterns of the equilateral-triangle cavity with a 935 nm side length. (a) CL spectrum of the cavity. The inset image is the SEM picture of the cavity. The spectrum from 400 to 650 nm was collected near the vertex, and the spectrum from 650 to 900 nm was collected at the center of the cavity (the arrow indicates the break). (b–d) Typical monochromatic CL images at wavelengths 818, 580, and 452 nm in vacuum, respectively. The brightness corresponds to the emitted photon intensity. (e–g) Simulated mode patterns. Scale bars are 500 nm.

Q-factors are attributed to the ultra-smoothness and high aspect ratio of the cavity structures fabricated via our technique.

The decreased roughness results in the increase of propagation length,^[3] which is very important to a large cavity. For example, more resonant modes are formed in a cavity with side length of 2 μm (Figure 4a). The electron beam is scanned from the vertex to the centre of the cavity (inset of Figure 4a) with a scan step of 180 nm, and the excited

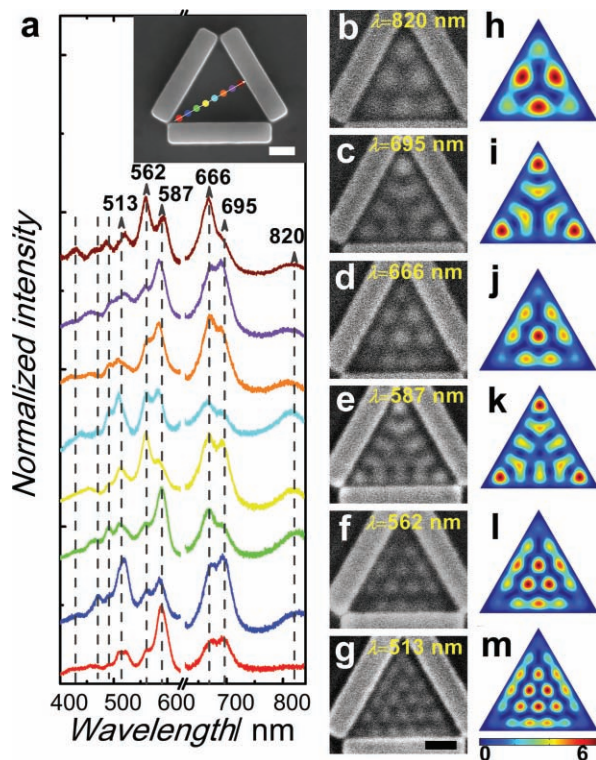


Figure 4. CL spectra and mode patterns of the equilateral-triangle cavity with a 2 μm side length. (a) CL spectra for the electron beam excited from the vertex to the middle point of opposite side of the cavity with a step size of 180 nm. The colour of the spectra corresponds to the different collected positions that are indicated in the same colour in the SEM image of the cavity (inset). Spectra are offset vertically for clarity. The breaks at 625 nm indicate that the spectra were collected twice at the same position due to the limit measuring range of the spectroscopy. (b–g) Monochromatic CL images at six resonant wavelengths in (a). (h–m) Simulated mode patterns. Scale bars are 500 nm.

spectra at each point are collected and shown in Figure 4a. Nine distinct resonant peaks with wavelengths of 820, 695, 491, 666, 587, 562, 513, 471, and 431 nm, are observed in the measurement range. Among them, the lowest six modes were imaged via monochromatic CL mapping at the corresponding peak wavelengths are shown in Figure 4b–g. These modes can be determined by comparison with theoretical mode patterns for the boundary condition $E = 0$, as shown in Figure 4h–m. The plasmonic modes of resonance wavelengths at 820 and 695 nm are degenerate, and they are assigned to the degeneration of modes (1, 7)/(3, 5) and (2, 8)/(3, 7), respectively. The modes of resonance wavelengths at 666, 562, and 513 nm are nondegenerate and correspond to the plasmonic modes (1, 13), (1, 11), and (1, 9), respectively. Figure 4k is the theoretical simulation of the mixed mode (2, 10) and (3, 9) (Supporting Information, Figure S6), which is very similar to the mode in Figure 4e. The difference in the resonant wavelengths of modes (2, 10) and (3, 9) is ~ 10 nm. The ultra-smoothness of the silver surface and the high reflectivity enable the formation of very clear SPP modes even in a large equilateral-triangular silver plasmonic cavity with a 2 μm side length and 300 nm height reflectors.

Table 1. Comparison of various TS methods.

Template	RMS roughness [nm]	Fabrication process	Controllable nanostructure (flexibility)	Aspect ratio	Reference
Mica	0.2–0.5	Simple	No	NA	[14,15]
FIB patterned mica	1.5	Complex	Yes(yes)	5	[16]
NSL [a] patterned mica	0.3–0.6	Simple	Yes(no)	NA	[17]
EBL-patterned PMMA	0.55–0.88	Simple	Yes(yes)	>20	This work

[a] Nanosphere lithography

A comparison of the traditional TS and our approach is listed in Table 1, which shows that our approach is very suitable for the fabrication of plasmonic structures with an ultra smooth surface, a high aspect ratio, complexity and flexibility. Several non-template stripping techniques were also used to fabricate equilateral-triangle cavities and the experimental results show the advantages of our method (Supporting Information, Figure S7–17). The influence of the height of the nanocavity was also investigated (Supporting Information, Figure S18–20). These results demonstrate that the ultrasmooth surface and the large height of the metal reflectors are two indispensable factors to obtain clear resonant modes in the nanocavities.

In summary, the TS method combined with PMMA as a template was successfully used to create extraordinarily smooth metal nanostructures with a desirable feature size and morphology for plasmonics and metamaterials. The advantages of this method, including the high resolution, precipitous top-to-bottom profile with a high aspect ratio, and three-dimensional characteristics, make it a unique technology for the fabrication of integrated metallic structures, and is very suitable for the fabrication of plasmonic structures, especially for subwavelength field confinement. It is reasonable to anticipate that our methodology can be applied to a wide variety of plasmonic applications due to its easy fabrication and flexibility.

Experimental Section

EBL and characterization: EBL was performed using SEM equipped with a lithography attachment (Raith Elphy Plus). The morphology of the fabricated patterns was characterized by SEM (FEI company, DB235 and Quanta 200F), and the roughness of surface was measured by AFM (Seiko SPI3800N, tapping mode).

CL measurements: Spatially and spectrally resolved CL measurements and CL imaging of the resonant plasmonic modes of the cavities were carried out by combining an SEM (FEI Quanta 200F) and a CL (Gatan Mono CL 3+) detection system. A 30 keV highly localized electron beam with a beam diameter of ~ 5 nm from a thermal field-emission gun source went through a 1 mm-diameter hole in a parabolic mirror above the sample holder and then impinged on the silver surface. The parabolic mirror with an off-axis focus effectively collected the light emitted from silver surface when the irradiated area of the metal was at the focus. Then, light was coupled to a charge-coupled device array detector through a monochromator. The measured CL spectrum was acquired at a fixed point with an exposure time of 16 s. This technique allows for a high localization of the SPP source, and its resolution is only limited by the finite size of the focused electron beam. The emission spectra include the transition radiation emission and the light decoupled from

the SPPs.^[25] For accuracy, the CL spectra are corrected for the response of the detection equipment by subtracting the background emission spectra of unstructured silver that is located far away from the structured silver. For monochromatic imaging, the electron beam homogeneously scanned over a chosen area in a scanning mode of operation, and the emitted light was coupled through the grating monochromator at selected wavelengths with a spectral passband ~30 nm. Each pixel in the monochromatic image corresponded to a different position of the electron beam, and the intensity of the pixel was proportional to the detected emission intensity of the spot when it was impinged by the electron beam.^[26,27] Secondary electron and monochromatic CL images were obtained simultaneously.

Supporting Information

Supporting Information is available from the Wiley Online Library or from the author.

Acknowledgements

This work was supported by NSFC (Nos. 10804002, 90606023, 10574003, and 10523001), MOST (Nos. 2007CB936202 and 2009CB623703), and the Research Fund for the Doctoral Program of Higher Education (RFDP), Ministry of Education, P. R. China.

Received: April 13, 2010

Revised: May 17, 2010

Published online: August 23, 2010

-
- [1] H. Raether, *Surface Plasmons on Smooth and Rough Surfaces and on Gratings*, Springer: Berlin, **1988**.
- [2] W. L. Barnes, A. Dereux, T. W. Ebbesen, *Nature* **2003**, *424*, 824.
- [3] P. Nagpal, N. C. Lindquist, S. H. Oh, D. J. Norris, *Science* **2009**, *325*, 594.
- [4] E. Ozbay, *Science* **2006**, *311*, 189.
- [5] A. Polman, *Science* **2008**, *322*, 868.
- [6] R. F. Oulton, V. J. Sorger, T. Zentgraf, R. M. Ma, C. Gladden, L. Dai, G. Bartal, X. Zhang, *Nature* **2009**, *461*, 629.
- [7] S. I. Bozhevolnyi, V. S. Volkov, E. Devaux, J. Y. Laluet, T. W. Ebbesen, *Nature* **2006**, *440*, 508.
- [8] H. Ditlbacher, J. R. Krenn, G. Schider, A. Leitner, F. R. Aussenegg, *Appl. Phys. Lett.* **2002**, *81*, 1762.
- [9] J. T. van Wijngaarden, E. Verhagen, A. Polman, C. E. Ross, H. J. Lezec, H. A. Atwater, *Appl. Phys. Lett.* **2006**, *88*, 221111.
- [10] C. E. Hofmann, E. J. R. Vesseur, L. A. Sweatlock, H. J. Lezec, F. J. García de Abajo, A. Polman, H. A. Atwater, *Nano Lett.* **2007**, *7*, 3612.
- [11] E. Laux, C. Genet, T. Skauli, T. W. Ebbesen, *Nat. Photonics* **2008**, *2*, 161.
- [12] S. Y. Chou, P. R. Krauss, P. J. Renstrom, *Appl. Phys. Lett.* **1995**, *67*, 3114.
- [13] I. Divliansky, T. S. Mayer, K. S. Holliday, V. H. Grespi, *Appl. Phys. Lett.* **2003**, *82*, 1667.
- [14] M. Hegner, P. Wagner, G. Semenza, *Surf. Sci.* **1993**, *291*, 39.
- [15] P. Wagner, M. Hegner, H. J. Güntherodt, G. Semenza, *Langmuir* **1995**, *11*, 3867.
- [16] M. Graca, J. Turner, M. Marshall, S. Granick, *J. Appl. Phys.* **2007**, *102*, 064909.
- [17] W. Frey, C. K. Woods, A. Chilkoti, *Adv. Mater.* **2000**, *12*, 1515.
- [18] D. P. Fromm, A. Sundaramurthy, P. J. Schuck, G. Kino, W. E. Moerner, *Nano Lett.* **2004**, *4*, 957.
- [19] T. Atay, J. H. Song, A. V. Nurmikko, *Nano Lett.* **2004**, *4*, 1627.
- [20] J. C. Weeber, A. Bouhelier, G. Colas des Francs, L. Markey, A. Dereux, *Nano Lett.* **2007**, *7*, 1352.
- [21] S. C. Kitson, W. L. Barnes, J. R. Sambles, *Phys. Rev. Lett.* **1996**, *77*, 2670.
- [22] E. J. R. Vesseur, F. J. García de Abajo, A. Polman, *Nano Lett.* **2009**, *9*, 3147.
- [23] M. V. Bashevov, F. Jonsson, A. V. Krasavin, N. I. Zheludev, Y. Chen, M. I. Stockman, *Nano Lett.* **2006**, *6*, 1113.
- [24] H. C. Chang, G. Kioseoglou, E. H. Lee, J. Haetty, M. H. Na, Y. Xuan, H. Luo, A. Petrou, A. N. Cartwright, *Phys. Rev. A* **2000**, *62*, 013816.
- [25] G. Leveque, C. G. Olson, D. W. Lynch, *Phys. Rev. B* **1983**, *27*, 4654.
- [26] E. J. R. Vesseur, R. de Waele, M. Kuttge, A. Polman, *Nano Lett.* **2007**, *7*, 2843.
- [27] R. Gómez-Medina, N. Yamamoto, M. Nakano, F. J. García de Abajo, *New J. Phys.* **2008**, *10*, 105009.